


Three-Dimensional Topological Reconstruction of the Sensing Coil of a Fiber-Optic Gyroscope Using X-Ray Computed Tomography

Jérémie Pillon , Matthieu Collignon, Maxime Rattier, François Louf, Emmanuelle Peter, Pierre-Alain Boucard, and Hervé C. Lefèvre

Abstract—The quadrupolar winding of the sensing coil of a fiber-optic gyroscope (FOG) is a useful technique to reduce the thermal bias drift of this sensor. This technique, which is based on orthocyclic winding, contains complex non-axisymmetrical zones, for example layer transitions or crossovers. In this paper, a precise topological reconstruction of the sensing coil is proposed using X-ray computed tomography. Thanks to this reconstruction, the first layer role and its impact on the next layers are studied. Then, the quality of the winding is quantified using interest parameters to evaluate crossovers and layer transition fibers. Finally, winding defects, particularly the propagation of gaps from layer to layer that causes sinking fibers, are highlighted.

Index Terms—X-ray computed tomography, optical fiber coil, fiber-optic gyroscope (FOG).

I. INTRODUCTION

THE sensing coil is one of the crucial components of fiber-optic gyroscopes (FOG) [1]–[3], which measures rotation rate with Sagnac effect [4]. In the early works of D.M. Shupe, and more recently in the papers of F. Mohr, it was shown that a thermal loading applied on a sensing coil gives rise to a non-reciprocal effect that causes thermal bias drift so-called pure Shupe effect [5] and elasto-optic effects [6], [7]. By examining the mathematical expression of this effect, one can assume that if two points, at equal distance of the midpoint of the fiber, experience the same thermal and mechanical loading then there is no thermal bias drift. Hence winding methods have been developed to reduce this thermal bias drift. Many works compare

winding methods [7]–[10], and the best industrial trade-off is the orthocyclic quadrupolar winding (see Section II).

Recently, in [11], the authors use optical coherence tomography (OCT), which gives a 3D-image of the coil to inspect precisely local and overall coil quality. The X-ray computed tomography used in this paper has a much better resolution. The X-rays damage the optical properties of the fiber, whereas OCT is non-destructive. Thus, X-ray tomography is not applicable to the control of manufactured coils, but is useful to validate the quality of a winding technology.

X-ray computed tomography produces, like the OCT, a 3D-image of the sensing coil. In this paper, we propose to also reconstruct the fiber topology, which means to get the coordinates of the fiber center along the coil. Then, using mathematical tools, we aim at studying and quantifying the non-axisymmetric effects, the local defects, and their propagation along the winding.

This article is structured as follows. First, the studied object is presented, focusing on the geometry of the orthocyclic quadrupolar winding. The major geometrical defects of these coils will also be discussed (Section II). The principle of the topology reconstruction using X-ray computed tomography is presented in Section III. Thanks to this reconstruction, an analysis of the quadrupolar winding is proposed in Section IV. We will focus first on the first layer because it requires special attention in more than one aspect: any defect introduced by this inner layer can propagate and disrupt the winding. A bad S-shift on this base layer can lead to crossover drift on all other layers. Necessarily, the S-shifts of the first layer must be analyzed precisely (Section IV-A1). Second, the metrology of the first layer is essential and is presented in Section IV-A2. Ultimately, on the first layer, the slightest defect, for example, a gap, will propagate to the other layers and affect the winding (Section IV-A3). Then we will examine and quantify the non-axisymmetrical zones (crossovers in Section IV-B and layer transitions in Section IV-C), and finally, we will investigate local and overall defects (Section IV-D).

II. GEOMETRY AND COMMON DEFECTS OF QUADRUPOLAR WINDING

In a fiber-optic gyroscope, the optical fiber coil has a quadrupolar winding using the classical orthocyclic technique. More precisely, the optical fiber coil is an orthocyclic winding

Manuscript received December 8, 2020; revised March 8, 2021; accepted March 19, 2021. Date of publication March 24, 2021; date of current version July 16, 2021. (Corresponding author: Jeremie Pillon.)

Jérémie Pillon is with Université Paris-Saclay, ENS Paris-Saclay, CNRS, LMT - Laboratoire de Mécanique et de Technologie, 91190 Gif-sur-Yvette, France, and also with iXblue, 78100 Saint-Germain-en-Laye, France (e-mail: jeremie.pillon@ixblue.com).

Matthieu Collignon, Maxime Rattier, Emmanuelle Peter, and Hervé C. Lefèvre are with iXblue, 78100 Saint-Germain-en-Laye, France (e-mail: matthieu.collignon@ixblue.com; maxime.rattier@ixblue.com; emmanuelle.peter@ixblue.com; herve.lefevre@ixblue.com).

François Louf and Pierre-Alain Boucard are with Université Paris-Saclay, ENS Paris-Saclay, CNRS, LMT - Laboratoire de Mécanique et de Technologie, 91190 Gif-sur-Yvette, France (e-mail: francois.louf@ens-paris-saclay.fr; pierre-alain.boucard@ens-paris-saclay.fr).

Color versions of one or more figures in this article are available at <https://doi.org/10.1109/JLT.2021.3068605>.

Digital Object Identifier 10.1109/JLT.2021.3068605

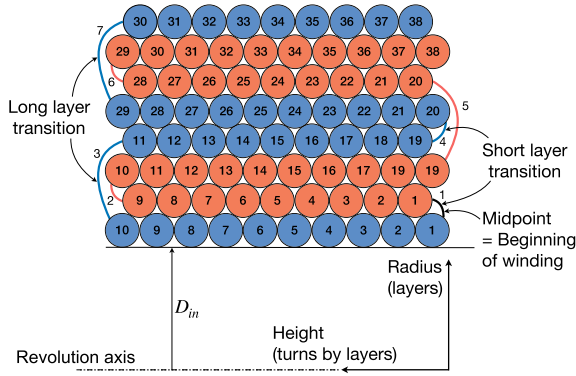


Fig. 1. Illustration of the theoretical orthocyclic quadrupolar winding with an hexagonal close-packed lattice with $N_z = 10$ turns on the first layer and $N_r = 8$ layers. The color of the fiber, blue or red, highlights the quadrupolar winding and reflects the two winding directions (referred to as A for blue fibers and B for red fibers) that start from the midpoint. The numbers into fibers correspond to the numbers of the turns in each direction of winding. The numbers next to the layer transitions correspond to fiber transition numbers.

following an hexagonal close-packed compact lattice (Fig. 1) over most of the perimeter. In the hexagonal close-packed zone, the fiber is not wound in a helix but parallel to the flanges, and then it shifts to form the next turn (Figs. 2(a) and 2(b)).

In the case of quadrupolar winding, the winding starts at the midpoint of the fiber length. This midpoint is put on the inside of the mandrel and pressed against the flange. Then, the fiber is alternatively wound with layers from either side of the midpoint. Therefore the elementary pattern of quadrupolar winding is composed of 4 layers (Fig. 1). The optical fiber coil is built layer by layer. Consequently, the quality of the first layer determines the quality of the coil and the quality of the FOG. The following analysis will be based on the chronology of coil formation, which means from the first to the last layer.

Hence, the geometry of a coil cannot be fully axisymmetric. There are intrinsic non-axisymmetrical zones that necessarily exist at each layer and each turn:

- 1) S-shift: in the first layer, due to orthocyclic winding, at each end of turn, the fiber shifts to form the next turn (Fig. 2(a)).
- 2) Crossover: from the layer number $i > 1$, between two turns, the fiber not only shifts but moves over two fibers of the underneath layer $i - 1$ and then settles into a new groove formed by adjacent fibers of the underneath layer. This non-axisymmetrical zone, that is called crossover, will be precisely studied and quantified in Section IV-B (Fig. 2(b)).
- 3) Layer transitions: it occurs at the end of each layer, to move the fiber up from layer n to the layer $n + 1$ or $n + 3$. Because of the pattern of the quadrupolar winding, we are going to distinguish the classical short transitions of orthocyclic winding (n to $n + 1$) and the additional long transitions of the quadrupolar technique (n to $n + 3$), as it is shown in Fig. 1. This non-axisymmetrical zone will be examined in Section IV-C (Fig. 2(c)).

In addition during a real winding some errors occur. These defects were partially addressed in the study on winding

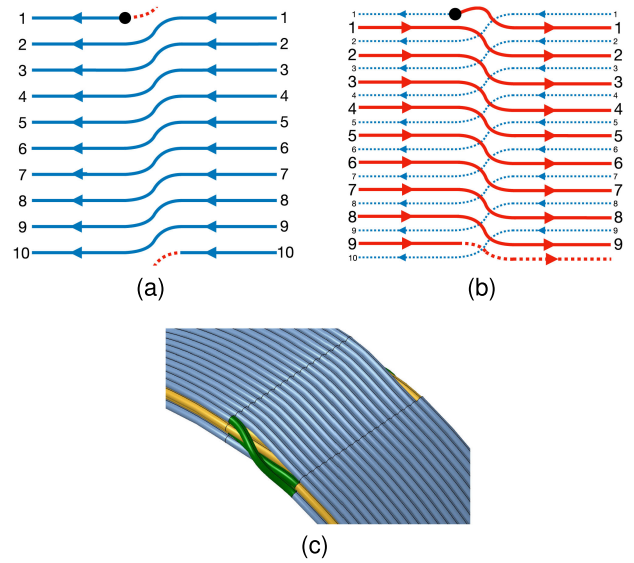


Fig. 2. Illustration of the three intrinsic non-axisymmetrical zones: (a) S-shift on the first layer which is characteristic of orthocyclic winding, (b) crossovers of the second layer (red line) over the first layer (blue dotted line) and the red dotted line is the beginning of the third layer, and (c) long layer transition fiber represented in green between the first and the fourth layer in blue and the second and the third layers are in yellow. At crossovers, the fiber overlaps two turns of the previous layer.

automation in [12], or more recently in [11]. These defects are illustrated in Fig. 3 and can be listed:

- 1) Gap: the distance between the mandrel flanges is not exactly $N_z \cdot d_{coat}$ as it should have been theoretically the case, where N_z is the number of turns and d_{coat} is the outer diameter of the optical fiber coating. There is a clearance δ_z to be able to pass through the layer transition fibers and the crossovers. This winding constraint creates a gap between some fibers in each layer.
- 2) Sinking fiber: due to axial clearance at the layer i , a fiber can fall into this gap at the layer $i + 1$. Thus this defect can propagate over several layers.

The study case we used is a free-standing coil with $N_r = 12$ layers, $N_z = 48$ turns and an inner diameter $D_{in} = 31.6 \text{ mm}$ that yields approximately a length of 60 m . The optical fiber used in this sensing coil has a double polymer coating with an outer diameter $d_{coat} = 169 \pm 2 \mu\text{m}$ and a silica cladding with a diameter $d_{clad} = 80 \mu\text{m}$. This optical fiber, produced by iXblue, is a classical tiger eye polarization-maintaining optical fiber. This 60 m coil is shorter than coils used in iXblue products to limit computational time.

III. PRINCIPLE OF THE THREE-DIMENSIONAL TOPOLOGICAL RECONSTRUCTION

X-ray computed tomography is an imaging technique that allows one to visualize all the components of an observed specimen. X-ray computed tomography is now widely used in many fields, including medical imaging or biology [13], [14], materials science [15], etc. Whatever the X-ray tomography technique, the basic principle is always the same [16]. An X-ray beam is sent to the sample mounted on a rotating platform. A series of N_θ

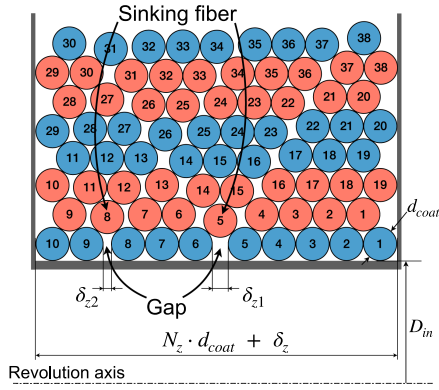


Fig. 3. Illustration of winding defects in quadrupolar winding following an hexagonal close-packed lattice. The clearance is noted δ_z and it is approximately equal to the outer diameter of the fiber coating ($\delta_z \approx d_{coat}$). Hence the distance between chuck flanges is $N_z \cdot d_{coat} + \delta_z$. Presence of two gaps of different sizes in the first layer between the fibers numbers 5 and 6 (δ_{z1}), and between the fibers numbers 8 and 9 (δ_{z2}). The sum of these two gaps δ_{z1} and δ_{z2} is equal to the clearance δ_z . The red fibers number 5 and 8 are sinking fibers created by the two gaps. In the case of the biggest gap, the defect propagates from layer to layer and creates gaps between fibers numbers 4 and 5, and between 5 and 6 in the second layer. Then these gaps cause other sinking fibers on the next layer and so on.

radiographs, corresponding to N_θ different angles of the sample (360° rotation in this case) in the X-ray beam, is recorded with a detector. A radiograph is obtained after making the average of 7 measurements during a 50 ms pause at a given angle, in order to decrease consequently the rotating vibration noise. Each radiograph is converted, using the Beer-Lambert law, to extract the projection of the absorption coefficient. The value of the absorption coefficient depends on the material density and on the atomic number. Consequently, the contrast of the images depends on the difference in the absorption coefficient of the different materials making up the sample. Finally, using a reconstruction algorithm [17] eF-X-CT provided by North Star Imaging, the 3D reconstructed volume is available. Fig. 4 describes this principle.

The X-ray computed tomography X-View X50-CT form North Star Imaging used in this study has a resolution of approximately $1.5\ \mu\text{m}$, and it allows us to distinguish the silica cladding from the surrounding polymer materials. However, this X-ray computed tomography can not distinguish coatings from coil glue because they have a similar density and atomic numbers.

The X-ray computed tomography yields a 3D image as final data. To analyze and quantify the orthocyclic quadrupolar winding and its defects, the coordinates of the fiber center all along the coil are necessary. This topological reconstruction is performed in three steps as illustrated in Fig. 5.

a) Step 1. Extraction of zones of interest: 2D cross-sectional views are extracted from X-ray computed tomography 3D image with an angular step of 0.1° . Then zones of interest (which means zones where fibers are detected) of each sectional view are extracted. Hence to have a complete revolution, and with this angular discretization, $N_\theta = 3600$ cross-sectional views are computed and extracted.

b) Step 2. Image binarization and centroids detection: In this step, cross-sectional view images are binarized in greyscale

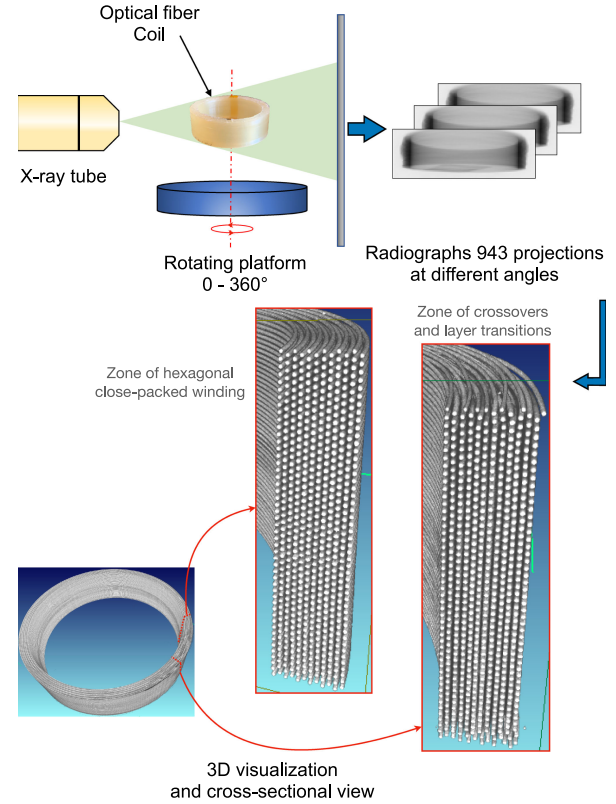


Fig. 4. Schematic view of the principle of X-ray tomography acquisition and reconstruction.

images by thresholding. The threshold is chosen as the mean of the histogram. Then on each cross-sectional view, circular blobs that correspond to the glass cladding are detected, and their centroids are saved. Finally, an examination process is carried out. Since the fiber diameter is $80\ \mu\text{m}$, and the resolution of the X-ray computed tomography is $1.5\ \mu\text{m}$, the glass cladding should be approximately 60 pixels. Any detected blobs with a size of $60 \pm 60\%$ pixels are blobs that are either artifacts or multiple fibers due to incorrect thresholding choices in the binarization process.

At the end of this step, the list of all fiber centroids of each cross-sectional view is available. Each variable of the list is noted s_i^j where i is the number of the detected centroid in the number j cross-sectional plan.

c) Step 3. Fibers association and filtering: This step will allow us to reconstruct the passage of the fiber in the coil by associating the centroids between the cross-sectional views. To do this, we start from the centroid corresponding to the last fiber denoted by i_0 in a given cross-sectional plan denoted by p_0 . Hence we denote by F this variable and we initialize it with $F_1 = s_{i_0}^{p_0}$. Next, we look for the centroid associated in the next cross sectional plan in an area equal to the coating diameter d_{coat} , and so on so forth until no more fibers are found. Then the same procedure is implemented on the other side to explore on the coil, which means we look for the centroid associated in the previous cross-sectional plan. We denote this variable G . Finally, by concatenating the two resulting vectors, we construct one vector, denoted $Fiber$, that stores the coordinates of the fiber

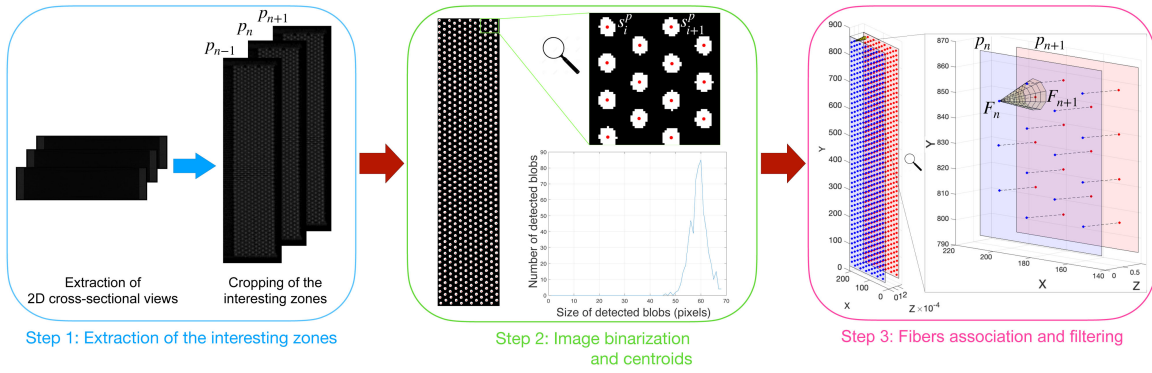


Fig. 5. Illustration of the principle of topological reconstruction of an optical fiber coil using X-ray computed tomography.

- 1: Initialization $F_1 \leftarrow s_{i_0}^{p_0}$
- 2: Initialization $j \leftarrow p_0$
- 3: **while** $\exists r, \|F_j - s_r^{j+1}\| < d_{coat}$ **do**
- 4: $F_{j+1} \leftarrow s_r^{j+1}$ {Exploration on one side}
- 5: $j \leftarrow j + 1$
- 6: **end while**
- 7: Initialization $G_1 \leftarrow s_{i_0}^{p_0-1}$
- 8: Initialization $k \leftarrow p_0 - 1$
- 9: **while** $\exists r, \|G_j - s_r^{k-1}\| < d_{coat}$ **do**
- 10: $G_{k-1} \leftarrow s_r^{k-1}$ {Exploration on the other side}
- 11: $k \leftarrow k - 1$
- 12: **end while**
- 13: $Fiber \leftarrow cat(G, F)$ {Concatenation of the two vectors}

Fig. 6. Fibers association algorithm.

along the coil. The algorithm to perform this step is detailed in Fig. 6.

This algorithm is based on the hypothesis that the previous binarization step is sufficiently efficient, which means:

- 1) all the fibers at each cutting plan are detected and there are no missing fibers
- 2) there is one and only one fiber in the search area.

Finally, we use a Butterworth filter to attenuate the reconstruction noise. Feedback allows us to affirm that the coiled fiber cannot have a variation greater than 0.1 mm for an angular distance of 0.1° . Hence this filter is configured with a cut-off frequency of 0.1 mm^{-1} and with an order of 5. The Butterworth filter does not decrease the resolution of the X-ray tomography. Hence after the reconstruction, the resolution of the reconstructed topology is still $1.5 \mu\text{m}$.

IV. EXPERIMENTAL RESULTS AND DISCUSSION

A. Study of the First Layer

The knowledge of the first layer is critical because the slightest tiny defect can spread over all layers. Hence this part presents the study of the various defects and non-axisymmetrical effects. Fig. 7(a) presents the first layer reconstructed in 3D.

1) *Fiber Shifts*: In the first layer, there is no crossover but only S-shifts, which means that there is only a shift in z -direction and not in r -direction. To study and visualize the S-shifts, we trace the turns of the first layer one by one in $\theta - z$ plan with

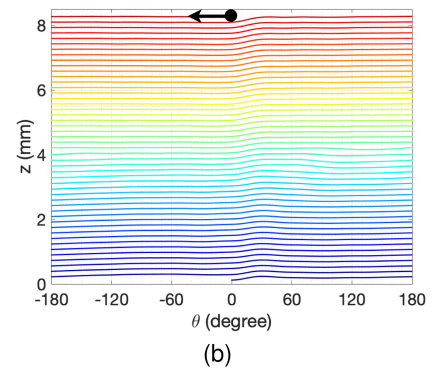
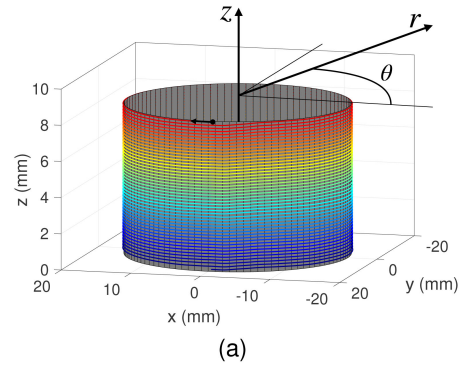


Fig. 7. First reconstructed layer: (a) 3D representation and (b) 2D representation of coordinates θ and z in $\theta - z$ plan. The first turn is represented in red and the last one in blue. The black circle corresponds to the start of the winding and the arrow indicates the direction of the winding.

the coordinate z of the fiber turns as a function of the angle θ (Fig. 7(b)).

Moreover, the second order derivative function $d^2z/d\theta^2$ (Fig. 9) is computed. With this function, it is possible to identify the center of the S-shift (noted α_Z) which is the inflection point (the angle where $d^2z/d\theta^2 = 0$) and the angular distance of the S-shift (noted $\Delta\alpha_Z$) which is the distance between the two points of maximum curvature (corresponding to the distance between the two spikes of the $d^2z/d\theta^2$ function), as illustrated with the first layer in Fig. 8.

By doing so for all turns (Fig. 9), it is possible to identify the values of these parameters: in this optical fiber coil first layer, the center of the shift fiber is $\alpha_Z \approx 16^\circ$, and the angular distance

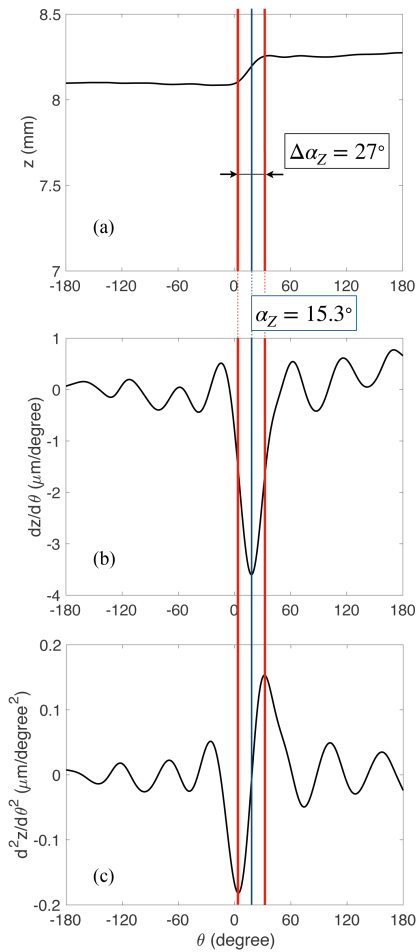


Fig. 8. First turn of the first layer in $\theta - z$ plan: (a) S-shift $z(\theta)$, (b) $dz/d\theta$ and (c) $d^2z/d\theta^2$. Identification, for the first turn, of interest parameters: the center of the shift α_Z (the angle where $d^2z/d\theta^2 = 0$) and the angular distance of the shift $\Delta\alpha_Z$ (the distance between the two spikes of the $d^2z/d\theta^2$).

is $\Delta\alpha_Z \approx 30^\circ$, with a low dispersion turn by turn. The value of the center of the shift has no specific meaning and depends on the chosen reference. Here the reference (0°) corresponds to the midpoint. However the variation of α_Z between layers will have an interesting interpretation.

Using Fig. 9, fibers of the first layer can be classified into three categories :

- 1) The first wound turns are pressed against the flange (the red fibers). Thus there are very well wound.
- 2) Then there is a zone where the fibers have a local gap (turquoise blue fibers), which can be due to the axial clearance. This zone will be also discussed in the next section.
- 3) Finally, the last wound turns inherit the previous defect but they are arranged properly.

2) *Inner Layer Metrology*: Theoretically, the first layer should form and generate a perfect cylinder of height $N_z \cdot d_{coat}$ and radius $(D_{in}/2) + (d_{coat}/2)$, excepted on the layer transition fibers. However, as highlighted in Fig. 10, the radius as a function of the angle position is not constant.

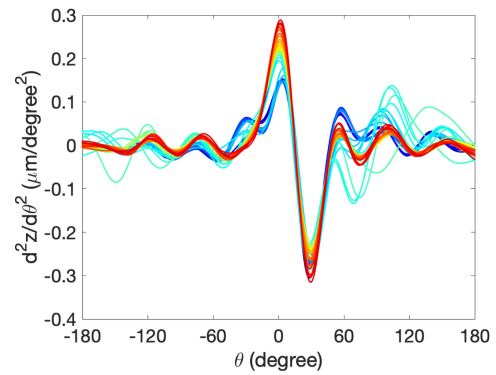


Fig. 9. Second order derivative function of the function $Z(\theta)$. The first turn is represented in red, and the last one in blue. The S-shifts of the turns are very well matched.

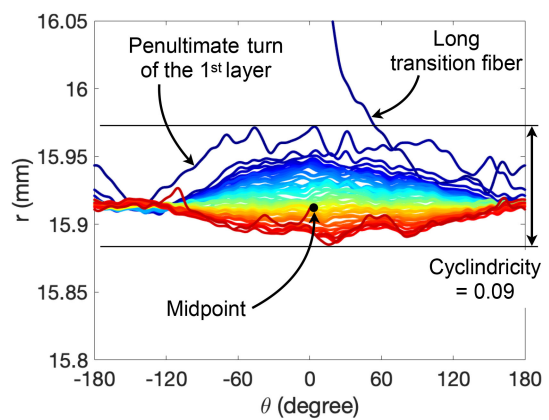


Fig. 10. First layer in $\theta - r$ plan turn by turn. The cylindricity appears as the envelope of all the turns. The circularity is the difference between the maximum and minimum radius for each layer. The first turn is represented in red, and the last one in blue. The penultimate turn is an example of an unexpected defect that can be called a climbing fiber.

Using the reconstructed first layer, one can generate and reconstruct the geometry and then perform the metrology of the first layer. The discrepancies between the real geometry and the theoretical geometry are presented in Fig. 11. It should be noted that the level of discrepancies is much higher than the resolution of the topological reconstruction ($\pm 1.5 \mu m$) and the tolerance on the fiber diameter ($\pm 1 \mu m$). Metrologically speaking, one can distinguish two shape tolerances:

- circularity: theoretically, the projected line in a diametrical cutting plan should be a circle. The circularity quantifies the radius deviation with this theoretical circle. In the case of cylinder tolerancing, the cylinder circularity is the maximum value of the circularity of each projected surface in a diametrical cutting plan. The circularity of a cutting plan is the difference between the maximum and minimum radius for each layer: for example, for the first layer, the radius varies between 15.927 mm and 15.885 mm , hence the circularity is $42 \mu m$. For the inner layer, the circularity can be evaluated at $63 \mu m$.
- cylindricity: the surface of the inner layer is located between two coaxial cylinders with different radii. The value of the cylindricity tolerance is the difference between the

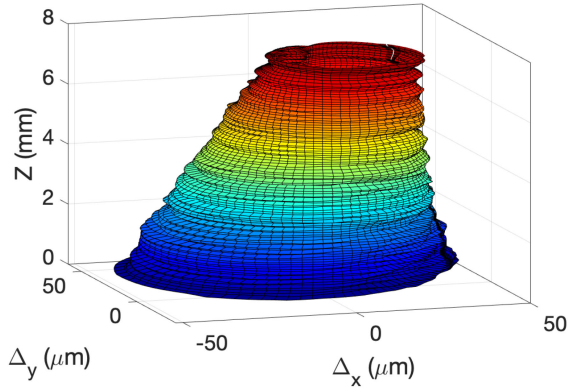


Fig. 11. Discrepancies between the model, a perfect cylinder, and the real generated surface. With this 3D-view the cylindricity is highlighted. Δ_x and Δ_y are respectively the difference between real and model in the x-axis and in the y-axis. These discrepancies may be due to mechanical tolerances of the mandrel. The first turn is represented in red and the last one in blue.

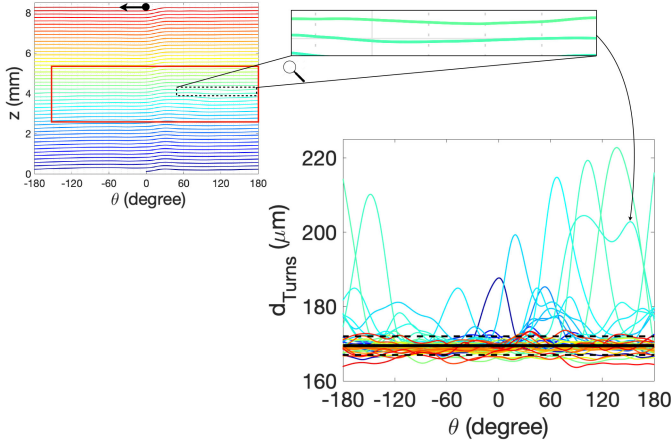


Fig. 12. On the left, the first turn in the $\theta - r$ plan with the identification of the gaps into the red rectangle and a zoom on one gap. On the right, the distance between two consecutive turns. The black curve represents the theoretical curve, which is constant and equal to the diameter of the fiber $d_{coat} = 169 \mu m$. The dashed curves symbolize the fiber diameter tolerance due to the resolution of the reconstruction and the manufacturing tolerance of the fiber. The distance between the first turn and the second turn on one side and the distance between the last turn and the penultimate turn on the other side are respectively represented in red and in blue.

value of these 2 radii. Using the Fig. 10, the cylindricity tolerance can be evaluated at $90 \mu m$.

These tolerance values could be due to geometrical defects and mechanical tolerances of the mandrel. However these inner layer defects do not degrade the winding quality but must be subtracted in order to distinguish defects due to inner layer from winding defects.

Finally, it is worth noting that the penultimate turn of the first layer, marked in Fig. 10, has a particular placement that reflects an unexpected defect. This defect was generated, probably, during manual winding by the following layers. This type of defect is called in the literature a climbing fiber .

3) *Other Defects in the First Layer:* In the first layer, the other defects will be reduced to gaps. To avoid this type of defect, we compute the distance between two consecutive turns (Fig. 12 at the right).

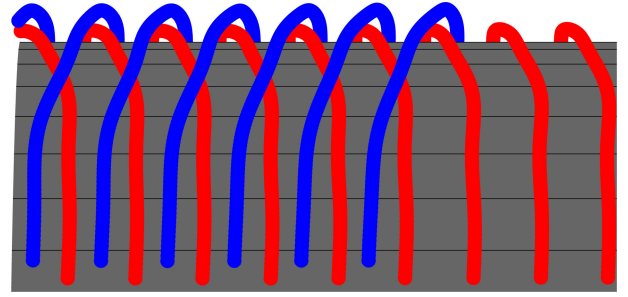


Fig. 13. Illustration of the crossovers of the second layer. The first layer is in red, and the second one in blue. The second layer overlaps two turns of the first layer to settle into a new groove formed by the layer underneath. Both the shift (z-direction) and the overlap (r-direction) are observed.

Theoretically, the distance between two consecutive fibers should be equal to the diameter of the fiber coating $d_{coat} = 169 \pm 2.5 \mu m$. However, some distances are not included in the tolerance bounds but not on the whole turn. Concerning the distances that are under the tolerance bounds, distance values are under the tolerance of the reconstruction. Therefore, it is not possible to conclude on this phenomenon. Concerning the distances above the tolerance bounds, this illustrates the gaps between the fibers. These gaps are very localized, few in number, and all located in the middle of the layer, symbolized by the red rectangle in Fig. 12.

Moreover, it is interesting to note that even in the shifting zone, the distances between two consecutive turns remain globally constant.

Finally, with this study, is it possible to evaluate experimentally the clearance δ_z which is $\delta_z = H - N_Z \cdot d_{coat}$ where H is the experimental height of the optical fiber coil determines in the Fig. 7(b) and $H = 8.276 mm$. Hence the clearance is equal to $\delta = 164 \mu m$ which is close to the value of the fiber coating diameter $\delta_z \approx d_{coat} = 169 \mu m$.

B. Crossover Inspection and Analysis

Contrary to the first layer, from the second layer, the fiber shifts not only in z-direction, but it also moves in r-direction (Fig. 13). Indeed the fiber moves over the fiber constituting a turn of the lower layer to settle into a new groove. To be more precise, as illustrated in Figs. 2(b) and 13, during the crossover, the fiber overlaps two turns of the lower layer. At crossover, there is a S-shift but also an overlap .

First, to analyze the crossovers, we will decompose the study by independently analyzing the S-shift in z-direction and the overlap in r-direction. To quantify the S-shift in z-direction, we implement the same interest parameters, namely the center of the shift α_Z and the angular distance of the shift $\Delta\alpha_Z$. To identify these parameters, we use the same technique as the one used to compute the pseudo-curvature $d^2z/d\theta^2$. The results for each layer are synthesized in Fig. 16.

Second, to analyze the crossovers in the r-direction, we will define parameters in the r-direction similar to those introduced for the z-direction. Consequently, we compute the radius as a function of the angle for each turn of each layer. The interest

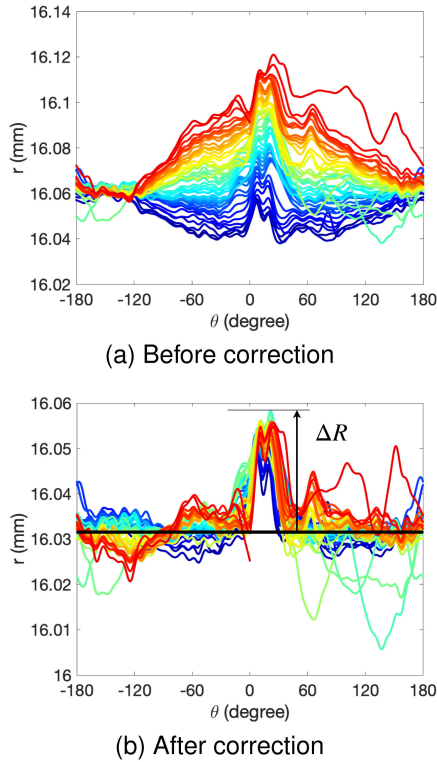


Fig. 14. All the turns of the second layer before (a) and after (b) the correction of the inner layer defects seen in Fig. 10 in the $\theta - r$ plan. The first turn is represented in red, and the last one in blue.

parameters are the center of the overlap α_R and the angular distance of the overlap $\Delta\alpha_R$. These parameters are identified using the pseudo-curvature in r -direction $d^2r/d\theta^2$. A new parameter will be added, which is the height of the overlap ΔR .

However, the first step is to distinguish the winding effects (crossovers, *etc.*) from the defects of the inner layer. Indeed, the impact of these defects can be found in all the layers. This problem is more valuable on the first layers because the height of the overlap is small in comparison of the inner layer defects and without a correction of these defects, the identification of the interest parameters is not possible (Fig. 14(a)). The corrected curves are obtained by subtracting the discrepancies between the model (a perfect cylinder) and the real generated surfaces (Fig. 11). The results of this correction of the inner layer defects are presented, for the second layer, in Fig. 14(b).

In this Fig. 14(b), one can remark that some turns, very localized and located in the middle of the layer, are situated below the theoretical radius. These turns are sinking fibers, and their angular positions correspond to the gaps created in the first layer (Fig. 12). There is also a unique fiber located at the beginning of the layer that is above the theoretical radius: it is a climbing fiber.

As already seen, in crossovers, the fiber overlaps two turns, and in the second layer, it is visible in Fig. 14 with a double hump in the curves. However, the higher the layer, the less visible this double hump is. For example in the 6th layer (Fig. 21(b)) and in the 12th layer (Fig. 22(b)) the double hump is not visible. It can

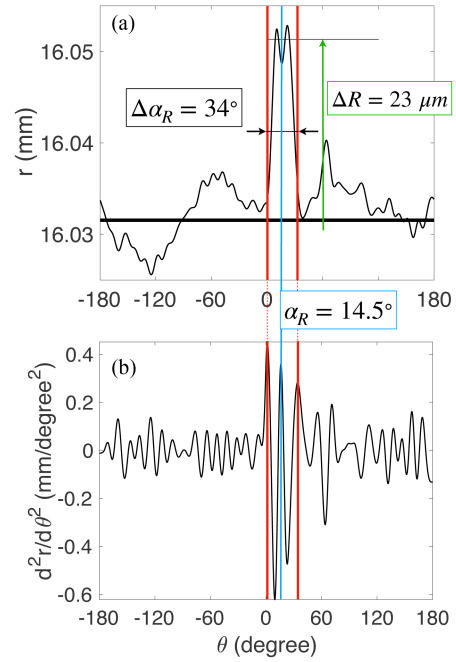


Fig. 15. 41th turn of the second layer in $\theta - r$ plan after inner layer correction: (a) $r(\theta)$ and (b) $d^2r/d\theta^2$. Identification of the interest parameters using the second order derivative function $d^2z/d\theta^2$.

be explained by the fact that the accumulation layer by layer is not perfect and so there is a smoothing which is done.

With this correction technique of the inner layer, the identification of the interest parameters is possible. An illustration of the identification of the parameters of interest, the center α_R , the angular distance $\Delta\alpha_R$ and the height ΔR of the overlap, are presented in Fig. 15.

By doing so for all turns and all layers, it is possible to give, in the crossover zones, the center α_R of the overlap in r -direction and its angular distance $\Delta\alpha_R$ for each layer as seen Fig. 16.

In crossover zones, the overlap in r -direction is more stable and has less variation than the S-shift in z -direction. It can be explained by the fact the overlap zone is wider than the S-shift zone. Furthermore, there is no correlation link between the variation and the dispersion on the overlapping center and the S-shift center. For all layers, the angular distance of the overlap is higher than the angular distance of shift, $\Delta\alpha_R > \Delta\alpha_Z$. That means that in the crossovers, the fiber first goes up, then shifts and overlaps, before going down.

Theoretically and using geometrical considerations, illustrated in Fig. 17, the height difference of the overlap increases due to layer-to-layer build-up and it is a function of the number of layer n_{layer} :

$$\Delta R(n_{layer}) = \left(1 - \frac{\sqrt{3}}{2}\right) \cdot d_{coat} \cdot (n_{layer} - 1) \quad (1)$$

The equation (1) of ΔR is true only if the interest parameters of the crossover, α_R , α_Z , $\Delta\alpha_R$ and $\Delta\alpha_Z$ are constants. Hence this expression represents the perfect pattern and then the maximum of height difference that is achievable. Since the parameters of interest are not constant, the layer to layer build-up is not

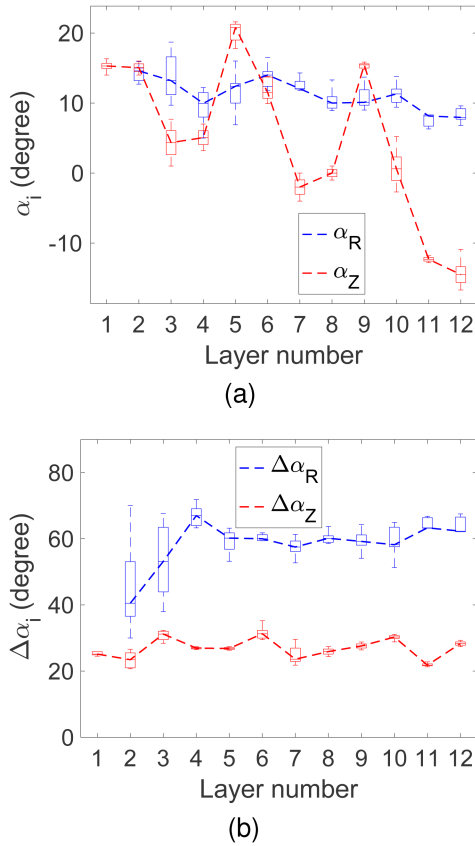


Fig. 16. Crossover characterization with two parameters of interest: (a) the angle corresponding to the center of the S-shift α_Z and the center of the overlap α_R and (b) the angular distance of the S-shift $\Delta\alpha_Z$ and the angular distance of the overlap $\Delta\alpha_R$. In the second layer, an angular distance of $\Delta\alpha_R = 52^\circ$ corresponds to a length of 14.55 mm , and in the last one, an angular distance of $\Delta\alpha_R = 62.3^\circ$ corresponds to a length of 19.02 mm . Box plots represent the dispersion between turns of the same layer. The bottom and top of each box are the 25th and 75th percentiles of the sample, respectively. The line in each box is the sample median. Lines extending from the boxes (whiskers) are the maximum and minimum values of the sample. Dashed lines connect the turn medians.

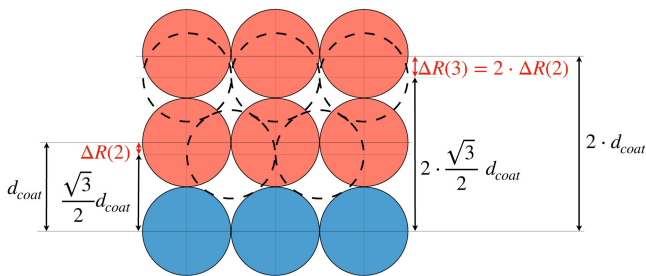


Fig. 17. Illustration of the theoretical geometry of the three first turns during the local overlap (r-direction) in the crossover zone. Fibers in dashed line represent the fibers in the hexagonal close-packed zone out of the cross-over zone. The height difference of the overlaps sums up layer by layer.

perfect, and the height of the overlap smooths throughout the layers. This explain the discrepancy observed in Fig. 18 between the experimental height and the theoretical value.

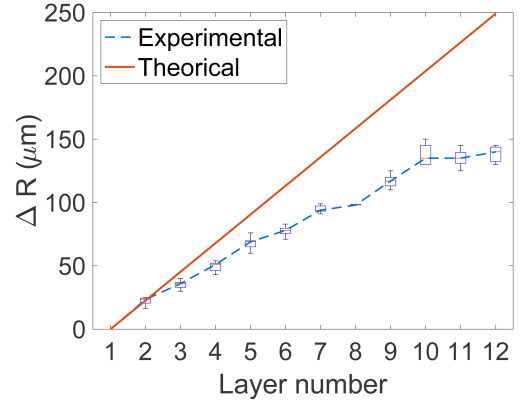


Fig. 18. Comparison of the height of the overlaps in the crossovers between the theoretical curve given by the equation (1), and the experimental curve. The box plots represent the dispersion between turns of the same layer following the same definition as in Fig. 16. The dashed line connects the turn medians.

To conclude this part, after the correction of the layers in r-direction by the inner layer defects, we computed the 5 parameters of interest. The 4 angular parameters are not constant. Consequently, they reveal a slight drift of the crossover zone through the layers. This angular parameter drift causes a smoothing of the crossover in r-direction. Therefore a discrepancy between the experimental height of the overlap and the theoretical geometry appears. However, the crossover does not present any collapse or defects that could lead to degrade considerably the performance of the FOG sensing coil.

C. Layer Transition Analysis

Layer transitions occur at the end of each layer to move the fiber up from layer n to the layer $n + 1$ or $n + 3$ for respectively short layer transition or long layer transition as it is was seen in Fig. 1 and as it is highlighted in Fig. 19(b).

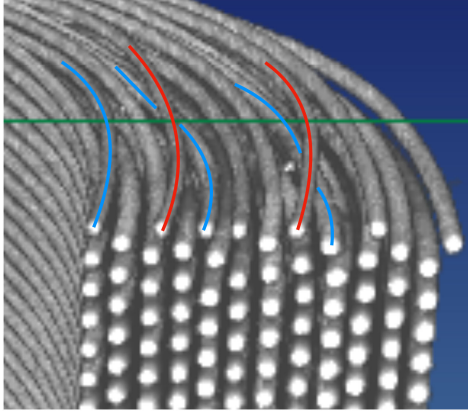
To study the layer transition fibers, we compute their lengths by distinguishing the short and the long layer transitions in Fig. 20.

Layer transition fibers number 5 and 9 are on the side of the flange where turns are very well wound as described in the section IV-A1. However, transition fibers number 3, 7 and 11 are on the other side, where the winding is less tidy. Hence the alternation of the long transition fibers can be explained by the fact that on the flange side, it is easier to move two layers up than on the other side because of the quality of the winding.

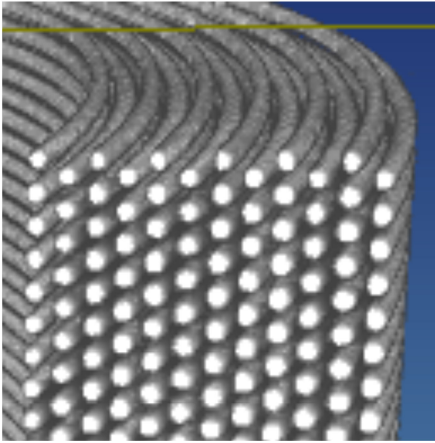
D. Other Local and Overall Defects

In this part, first, we examine gaps and sinking fibers. Then, we analyse the length of each turn and the length symmetry. Finally, we propose an overall quantification of winding quality outside of the crossover zones.

1) *Gaps and Sinking Fibers*: To study these defects, we use two couples of curves. First we compute the distance between two consecutive turns of the 5th layer and the representation of the 6th layer in the $\theta - r$ plan (Fig. 21). Second, we compute the distance between two consecutive turns of the 11th layer and the representation of the 12th layer in the $\theta - r$ plan (Fig. 22).



(a)



(b)

Fig. 19. (a) Magnified view of the zone of crossovers and layer transitions. Because of crossovers, the turns do not follow an hexagonal close-packed lattice anymore. Blue lines highlight the short transition fiber number 1, 4 and 8, and red lines highlight the long transition fibers number 5 and 9. (b) As a comparison, a similar magnified view of the hexagonal close-packed zone along almost 90% of the perimeter.

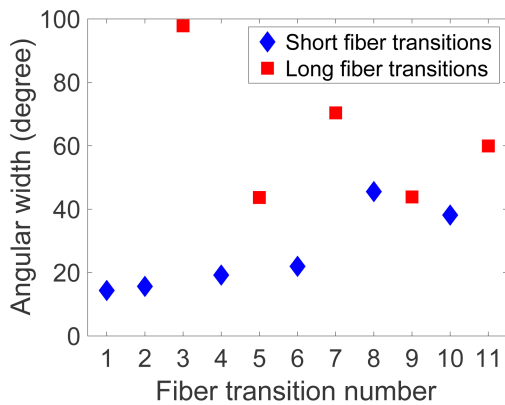


Fig. 20. The angular distance of the transition fibers. The layer transition fibers are numbered in the winding order as presented in Fig. 1. For example, the fiber transition number 1 is the short fiber that goes from layer number 1 to layer number 2 and the fiber transition number 3 is the long transition fiber that goes from layer number 1 to layer number 4. The first short transition fiber has an angular distance of 14.4° that corresponds to a length of 4 mm , and the last long one has an angular distance of 60° that corresponds to a length of 18 mm .

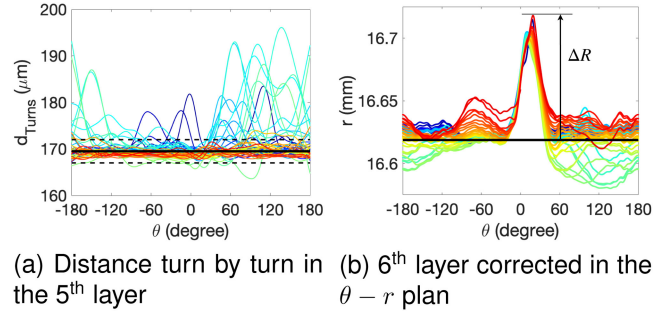


Fig. 21. Illustration of the transition between the 5th and the 6th layer: the gaps in the 5th layer (a) cause sinking fibers in the 6th layer (b). Both are localized at the same angular position.

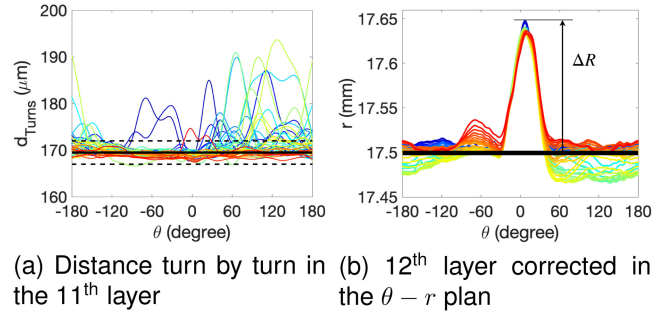


Fig. 22. Illustration of the transition between the 11th and the 12th layer: (a) the gaps in the 11th layer cause (b) sinking fibers in the 12th layer. Both are localized at the same angular position.

If we compare the Figs. 12, 21(a) and 22(a), we can notice that the higher the layer number, the more the gap number increases. The same observation can be made for the sinking fibers: the higher the layer number, the more the number of sinking fibers increases. This remark is in agreement with the fact that gaps cause sinking fibers. Moreover, it is interesting to highlight that the gap width does not increase as the layers are built up. Finally, by examining Figs. 21(b) and 22(b), fibers fall of approximately $60\ \mu\text{m}$ maximum. This value is the same for the 6th and the 12th layers. This value is not sufficient for the fiber to fall into the lower layer.

We can conclude that the gaps created in the first layer have propagated and cause sinking fibers. Moreover, their number increases proportionally with the layer number. Nevertheless, width of the gaps does not increase with the layer and remains constant.

2) *Length of Each Turn and Length Symmetry*: Theoretically, the length of each turn l_{turn} of a given layer can be expressed as a function of coil and fiber parameters (D_{in} and d_{coat}) and depends of the layer number n_r as follows:

$$l_{turn} = 2\pi \left[D_{in} + \frac{d_{coat}}{2} + (n_r - 1) \frac{\sqrt{3}}{2} \right] \quad (2)$$

One can remark that this theoretical expression does not take into account cross-overs nor layer transitions.

Fig. 23 compares the experimental length of each turn with the theoretical length.

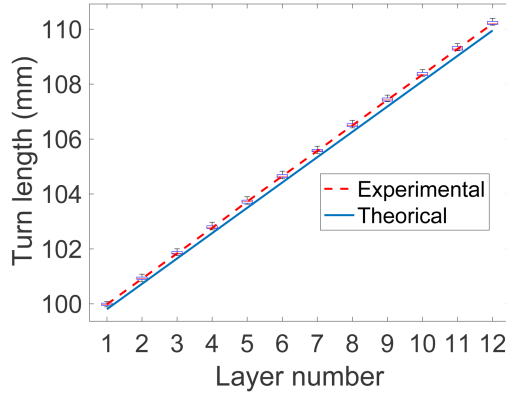


Fig. 23. Comparison between experimental and theoretical turn length as a function of layer number. Box plots represent the dispersion between turns of the same layer following the same definition as in Fig. 16. The red dashed line connects the turn medians.

First, a low dispersion between turns of a same layer is highlighted in Fig. 23. Moreover the dispersion is constant layer to layer. Indeed, the difference between maximum turn length and minimum turn length is approximatively evaluated at $250 \mu m$. Second, one can find small discrepancies between experimental and theoretical curves. The first explanation we can give is that theoretical curve does not take into account cross-overs nor layer transitions. Moreover, the median values of experimental turn lengths remain linear with the layer number, but with a different slope than the theoretical curve. Consequently, discrepancies are increasing layer by layer. The initial discrepancy in the first layer can be explained with the inner layer metrology pointed in the paragraph IV-A2.

Let us now consider what we call “length symmetry,” by comparing the length in both winding directions (referred to as A and B in Fig. 1). The length symmetry is another quite important indicator for the winding technology and it needs to be as small as possible. However, even if we neglect cross-overs and layer transitions, lengths in both winding directions, denoted L_A^{th} and L_B^{th} , can not be equal theoretically. Indeed, for example, on the last layer (direction A) there are $N_z - 1$ turns whereas on the penultimate layer (direction B) there are N_z turns. Moreover, the variation of radius between these two layers does not make it possible to compensate for the excess turn. Consequently length in direction B is longer than length in direction A . More precisely, L_A^{th} and L_B^{th} can be expressed, using arithmetic suites, as follows:

$$\begin{aligned}
 L_A^{th} = & 2\pi \cdot N_z \cdot \left\{ \frac{N_r}{4} R_1 \right. \\
 & + \left. \left(\frac{N_r}{4} - 1 \right) \left[4 + 2 \left(\frac{N_r}{4} - 2 \right) \right] \frac{\sqrt{3}}{2} d_{coat} \right\} \\
 & + 2\pi \cdot (N_z - 1) \cdot \left\{ \frac{N_r}{4} R_1 \right. \\
 & + \left. \frac{N_r}{4} \left[3 + 2 \left(\frac{N_r}{4} - 1 \right) \right] \frac{\sqrt{3}}{2} d_{coat} \right\} \quad (3)
 \end{aligned}$$

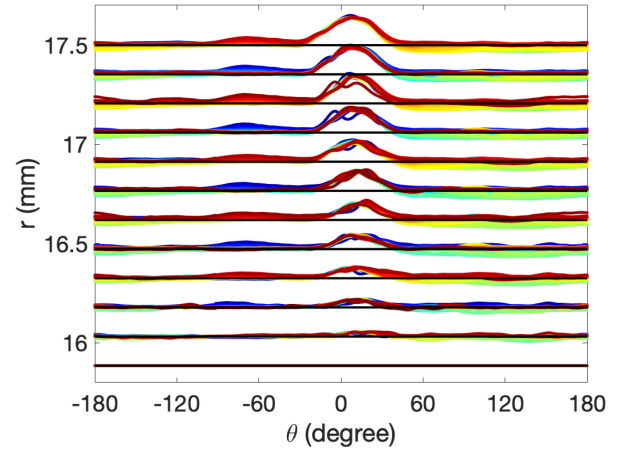


Fig. 24. Radius of all the turns of the layers in the $\theta - r$ plan. We can visualize the layer-to-layer increase of the height of the overlap ΔR in the crossover zones as highlighted in Fig. 18. We can also observe a very small θ -drift of the crossover zones as the layer number increase. Black lines symbolize the theoretical distance $(\sqrt{3}/2) d_{coat}$ between layers in hexagonal close-packed lattice. Layer transition fibers are not represented.

$$\begin{aligned}
 L_B^{th} = & 2\pi \cdot N_z \cdot \left\{ \frac{N_r}{4} R_1 \right. \\
 & + \left. \frac{N_r}{4} \left[2 + 2 \left(\frac{N_r}{4} - 1 \right) \right] \frac{\sqrt{3}}{2} d_{coat} \right\} \\
 & + 2\pi \cdot (N_z - 1) \cdot \left\{ \frac{N_r}{4} R_1 \right. \\
 & + \left. \frac{N_r}{4} \left[1 + 2 \left(\frac{N_r}{4} - 1 \right) \right] \frac{\sqrt{3}}{2} d_{coat} \right\} \quad (4)
 \end{aligned}$$

with $R_1 = R_{in} + \frac{d_{coat}}{2}$ with $R_{in} = \frac{D_{in}}{2}$ the inner radius of the coil.

Therefore difference in length symmetry $L_A^{th} - L_B^{th}$ is given by:

$$L_A^{th} - L_B^{th} = -2\pi \frac{N_r}{2} \cdot \frac{\sqrt{3}}{2} \cdot d_{coat} \quad (5)$$

We find back that the length of direction B is longer than the length of direction A . Hence for this studied coil $L_A^{th} - L_B^{th} = -5.6 \text{ mm}$, with $L_A^{th} = 29.8865 \text{ m}$ and $L_B^{th} = 29.8921 \text{ m}$. Using reconstructed topology, the difference in length symmetry is evaluated at -8.86 mm with the length in direction A $L_A^{exp} = 30.6888 \text{ m}$ and the length in direction B $L_B^{exp} = 30.6977 \text{ m}$. The discrepancies between experimental and theoretical lengths in each direction can be explained with the same reasons as those used for the turn length discrepancies. Indeed, theoretical approach does not take into account the additional lengths brought by cross-overs, and the inner layer defects.

3) *Towards an Overall Quantification of the Winding Quality:* Radially, and under geometric considerations, the distance between layers in close-packed zone is $(\sqrt{3}/2) d_{coat}$, and we want to verify experimentally if it is true or not. A greater distance indicates a lack of contact between two consecutive layers, which may be due to the presence of glue between them.

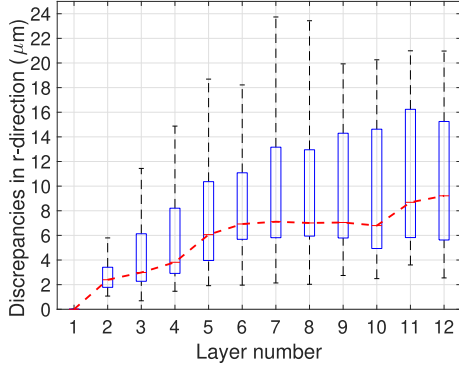


Fig. 25. Quadratic means of the distance between experimental radius and theoretical radius of each turn presented layer to layer. Box plots represent the dispersion between turns of the same layer following the same definition as in Fig. 16. The red dashed line connects the turn medians.

Fig. 24 presents the corrected radius of each turn of the optical fiber coil. One can distinguish the 12 layers and the overlaps in the r-direction at the crossovers.

To quantify this radial distance between the experimental fibers and the theoretical curves, we compute, in Fig. 25, the quadratic mean of the distance between the experimental radius and the theoretical radius turn by turn. This quadratic mean $d_{i,j}^R$ is defined for the turn i and the layer j , and between the angle θ_1 and θ_2 by:

$$d_{i,j}^R = \sqrt{\frac{1}{\theta_2 - \theta_1} \int_{\theta_1}^{\theta_2} (R_j^{th} - R_{i,j}^{exp})^2 d\theta} \quad (6)$$

with R_j^{th} is the theoretical radius at the layer j , $R_{i,j}^{exp}$ is the experimental radius, corrected by the inner layer, of turn i and layer j . Given that the crossover was studied previously, the angles θ_1 and θ_2 are chosen to exclude crossovers, consequently $\theta_1 = 50^\circ$ and $\theta_2 = 330^\circ$.

With Fig. 25, we verify two remarks made previously. First, the sinking fiber number is almost increasing proportionally with the layer number. Second, the fibers fall from a maximum value that changes only slightly between layers 5 and 12. To complete this remark, the evolution of the maximum values does not follow the same curve as the median. Moreover, one can observe that the minimum values of this quadratic mean distance are not equal to zero. However, these minimum values are smaller than the resolution (of the topological reconstruction and on the fiber diameter) which is $2.5 \mu\text{m}$. Consequently, it is not possible to conclude strictly on the contact or not of the fibers, layer by layer, and on the presence or not of glue between them.

Next, we compute the same quantity of interest but in z-direction (Fig. 26): the quadratic mean between the experimental height and the theoretical height. This quadratic mean $d_{i,j}^Z$ is defined for the turn i and the layer j between the angle θ_1 and θ_2 by:

$$d_{i,j}^Z = \sqrt{\frac{1}{\theta_2 - \theta_1} \int_{\theta_1}^{\theta_2} (Z_j^{th} - Z_{i,j}^{exp})^2 d\theta} \quad (7)$$

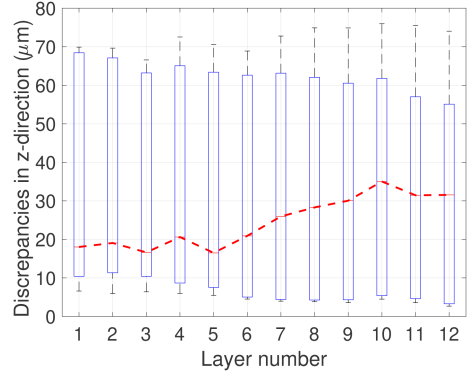


Fig. 26. Quadratic means of the distance between experimental height and theoretical height of each turn presented layer to layer. Box plots represent the dispersion between turns of the same layer following the same definition as in Fig. 16. The red dashed line connects the turn medians.

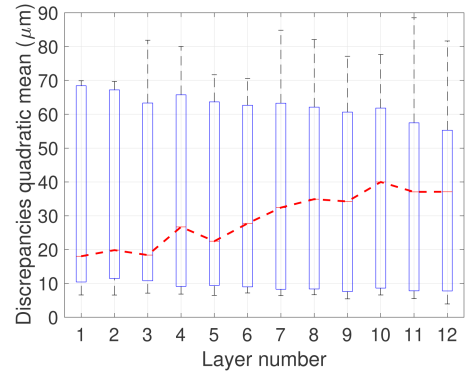


Fig. 27. Quadratic means of the 3D distance between experimental height and theoretical height of each turn presented layer by layer. Box plots represent the dispersion between turns of the same layer following the same definition as in Fig. 16. The red dashed line connects the turn medians.

with Z_j^{th} is the theoretical height at the layer j , $Z_{i,j}^{exp}$ is the experimental height of the turn i and the layer j . The angles θ_1 and θ_2 are the same values as previously shown.

The distance between the theoretical height and the experimental height increases with the layer number. Consequently, the number of gaps increases too. However, the dispersion between the turns remains almost constant, layer to layer. This observation means that the values of gaps also remain substantially constant. Moreover, it should be emphasized that there is a large dispersion of values within a layer and that this dispersion remains almost constant layer by layer. As reported in paragraph IV-A1, this dispersion is caused by the fact that fibers close to the flange are very well wound and thus, with a small quadratic mean distance, contrary to fibers on the opposite side.

Finally, we compute in Fig. 27 the quadratic mean of the 3D distance of the fiber between the experimental position and the theoretical position $d_{i,j}$. Position $d_{i,j}$ is defined for the turn i and the layer j between the angle θ_1 and θ_2 by:

$$d_{i,j} = \sqrt{\frac{1}{\theta_2 - \theta_1} \int_{\theta_1}^{\theta_2} [(R_j^{th} - R_{i,j}^{exp})^2 + (Z_j^{th} - Z_{i,j}^{exp})^2] d\theta} \quad (8)$$

Again, θ_1 is equal to 50° and θ_2 to 330° .

Fig. 27 allows us to conclude on the winding quality outside of the crossover zones. First, some residual dispersion exists between the turns of the same layer. This remark can be explained by the fact that the fiber is wound on the side resting on the flange or on the other side. However, the extent of these dispersions remains constant. Then the defects introduced in the first layer propagate layer to layer. Nevertheless, the maximum value of these defects remains constant. Therefore, the number of defects increases but their size decreases. However, given that the medians per layer are between $18\ \mu\text{m}$ and $40\ \mu\text{m}$, these defects are relatively small. Consequently, this studied coil is very carefully wound.

V. CONCLUSION

In this paper, we propose a new approach using X-ray computed tomography to visualize and reconstruct the three-dimensional topology of the sensing coil of a FOG. We inspect the winding quality and particularly the non-axisymmetrical effects. We focus on crossovers, gaps, and other local imperfections. We have developed interest parameters to quantify the quality and the defects of the winding. We highlight the fact that the winding quality of the first layer is especially critical and needs special attention. Indeed gaps in the first layer will cause sinking fibers and other gaps on the next one, and they will then propagate from layer to layer.

In this study, we only had access to the center of the cladding of the fiber and we have no information on the local deformations, nor the coatings, and the glue. One way to be able to distinguish the cladding from the coatings and the glue is to increase the contrast of the X-ray tomography between the different materials by injecting a contrasting product in the glue. Moreover, to determine if this study is robust and consequently extensible to any quadrupolar optical fiber coil, coils with more layers and a different number of turns would have to be studied.

Furthermore, knowing how defects are created, it is recommended to take special care of the first layer during winding.

Finally, it will be possible to propose numerical models of optical fiber coil based on this topological reconstruction.

ACKNOWLEDGMENT

This work was performed using HPC resources from the “Mésocentre” computing center of CentraleSupélec and École

Normale Supérieure Paris-Saclay supported by CNRS and Région Île-de-France (<http://mesocentre.centralesupelec.fr>). The authors would like to thank Sylvain Benard from iXblue in Lannion for the manufacture of this studied coil with such care and precision.

REFERENCES

- [1] E. Udd and M. J. Digonnet, *Design and Development of Fiber Optic Gyroscopes*. Bellingham, WA, USA: SPIE Press, 2019.
- [2] H. C. Lefvre *et al.*, “The fiber optic gyro ‘adventure’ at photonics, ixsea and now ixblue,” in *Proc. Opt. Waveguide Laser Sensors, Int. Soc. Opt. Photon.*, 2020, Art. no. 1140505.
- [3] H. C. Lefvre, *The Fiber-Optic Gyroscope*, 2nd ed. Norwood, MA, USA: Artech-House, 2014.
- [4] G. Sagnac, “L’ether lumineux demontre par l’effet du vent relatif d’ether dans un interferometre en rotation uniforme,” *CR Acad. Sci.*, vol. 157, pp. 708–710, 1913.
- [5] D. M. Shupe, “Thermally induced nonreciprocity in the fiber-optic interferometer,” *Appl. Opt.*, vol. 19, no. 5, pp. 654–655, 1980.
- [6] F. Mohr and F. Schadt, “Error signal formation in fogs through thermal and elastooptical environmental influences on the sensing coil,” in *Proc. Symp. Gyro Technol.*, 2011, pp. 2–2.
- [7] F. Mohr, “Thermooptically induced bias drift in fiber optical Sagnac interferometers,” *J. Lightw. Technol.*, vol. 14, no. 1, pp. 27–41, 1996.
- [8] N. J. Frigo, “Compensation of linear sources of non-reciprocity in Sagnac interferometers,” in *Proc. Fiber Opt. Laser Sensors I, Int. Soc. Opt. Photon.*, 1983, pp. 268–271.
- [9] C. M. Lofts, P. B. Ruffin, M. D. Parker, and C. C. Sung, “Investigation of the effects of temporal thermal gradients in fiber optic gyroscope sensing coils,” *Opt. Eng.*, vol. 34, no. 10, pp. 2856–2864, 1995.
- [10] K. Hotate and Y. Kikuchi, “Analysis of the thermo-optically induced bias drift in resonator fiber optic gyro,” in *Proc. Fiber Opt. Sensor Technol. II, Int. Soc. Opt. Photon.*, 2001, pp. 81–88.
- [11] Z. Li, Z. Meng, L. Wang, T. Liu, and S. X. Yao, “Tomographic inspection of fiber coils using optical coherence tomography,” *IEEE Photon. Technol. Lett.*, vol. 27, no. 5, pp. 549–552, Mar. 2015.
- [12] T. L. D. Fazio, K. L. Belsley, R. H. Smith, G. Shank, and W. H. Culver, “Development issues for automating quadrupole-pattern optical-fiber coil-winding for fiber-optic gyro manufacture,” in *Proc. IEEE Int. Conf. Robot. Automat.*, 1994, pp. 202–207.
- [13] A. Momose, T. Takeda, Y. Itai, and K. Hirano, “Phase-contrast x-ray computed tomography for observing biological soft tissues,” *Nat. Med.*, vol. 2, no. 4, pp. 473–475, 1996.
- [14] W. A. Kalender, “X-ray computed tomography,” *Phys. Med. Biol.*, vol. 51, no. 13, p. R 29, 2006.
- [15] J. Baruchel, J.-Y. Buffiere, and E. Maire, “X-ray tomography in material science,” 2000.
- [16] A. C. Kak, M. Slaney, and G. Wang, “Principles of computerized tomographic imaging,” *Med. Phys.*, vol. 29, no. 1, pp. 107–107, 2002.
- [17] S. R. Stock, *Microcomputed Tomography: Methodology and Applications*. Boca Raton, FL, USA: CRC Press, 2019.